3

Study of Schottky Barrier Height using Metal/TiO_2 nanoplates for Hydrogen Gas Sensing

This chapter focuses on the temperature dependent electrical transport properties of different metal contacts on TiO_2 nanoplates and their hydrogen gas sensing behaviour. Barrier heights between different metals and TiO_2 are calculated using *I-V* characteristics at different temperature. Due to dissimilar work function of different metals such as Al, Ag, Ni, and Au, the barrier height should be different when these metals make contact with TiO_2 (n-type). Thus, the metal's work function and electron affinity of TiO_2 provides the Ohmic/Schottky contacts. Later, hydrogen gas sensing studies which are based on Schottky barrier height of different metal contacts on TiO_2 nanoplates at different working temperature were carried out. TiO_2 nanoplates have been deposited on Si-substrate and their structural, morphological, and electrical characterizations have been described systematically. Therefore, different metal contacts are fabricated on the surface of TiO_2 nanoplates to observe the hydrogen gas sensing behaviour at different temperature. The maximum sensing response has been obtained by Au contacted TiO_2 nanoplates as compared to other sensors at same parameters. The increased hydrogen sensing response is mainly due to highest Schottky barrier height for Au contacted TiO_2. Moreover, possible gas sensing mechanism is described at the end of the chapter.

3.1 INTRODUCTION

Gas sensors have several applications in automotive, environment monitoring, safety, space, and domestic purposes to recognize flammable and toxic gases [Timmer *et al.,* 2005; Liu *et al.,* 2012]. Large depletion of hydrocarbon fuels due to their extensive use in on-board vehicle creates the need of substitutes like hydrogen, which is also known as a futuristic fuel [Lupan *et al.,* 2012]. It is well known that the hydrogen combines with air quickly making it highly flammable. Thus, one needs to detect hydrogen precisely to avoid risks associated with human lives [Soo *et al.,* 2010]. The main objective is to use hydrogen sensors at low operating temperature for safety and low power consumption. MO_x based nanostructures are largely used in gas sensing because of their high sensitivity, small response time, and good stability, which is due to high surface aspect ratio of MO_x nanostructures [Li *et al.,* 2007]. Anatase phase TiO_2 nanostructures is widely utilized in hydrogen sensing due to their low cost, high chemical and thermal stability under the sensor's operating conditions [Zakrzewska *et al.,* 2017]. Interestingly, sensing response of hydrogen sensor could be influenced by the following factors: (i) High surface to volume ratio increase the interaction of hydrogen gas on the surface [Korotcenkov *et al.,* 2008; Kadir *et al.,* 2015]. (ii) Some catalyst metal dissociates the H_2 molecules at the interface [Pandis *et al.*, 2007; Wu *et al.,* 1993]. Ionized H_2 atoms form a dipole layer between the interface, which produces an electric field; resulting in the reduction of effective barrier height as well as metal work function [Pandis *et al.,* 2007]. (iii) Schottky barrier height at the interface of metal/TiO_2 interface; barrier height is largely affected by the H_2 concentration, which leads to decrease in barrier height and increase in sensitivity during the exposure of H_2 gas.

The Schottky barrier height (ϕ_B) between metal and semiconductor can be determined by thermionic emission theory in forward bias [Ranwa *et al.*, 2014] and Bardeen model in reverse bias [Rakhshani *et al.*, 1998]. Rahbarpour *et al.* [Rahbarpour *et al.*, 2013] grew Ag-TiO_2-Ti Schottky type diode, and found a transition from Schottky behavior in clean air to ohmic behaviour in pure H_2 at 300°C. It was suggested that this transformation was due to large reduction in barrier height and change in the metal work function of H_2 gas. Ling *et al.* [Ling *et al.*, 2016] investigated Au-TiO_2 nanotubes Schottky diode and observed higher relative response towards H_2 in reverse bias voltage. Researchers such as Babaei *et al.* [Babaei *et al.*, 2011] have shown effective barrier height reduction of 0.17 eV, 0.25 eV, and 0.57 eV with Ag, Au, and Ti electrodes, respectively on TiO_2 nanostructure from hydrogen contaminated air to clean air. Kandasamy *et al.* [Kandasamy *et al.*, 2013] Pt/TiO_2 thin film layered was fabricated for hydrogen sensing, and highest change in effective barrier height ($\Delta\phi_B$) was found to be ~0.125 eV for 1% H_2 concentration. Decrease in barrier height was due to the reduction in Pt work function caused by absorption of hydrogen. In this chapter, Metal/TiO_2 (M/TiO_2) nanoplates have been fabricated and the effect of Schottky barrier height of different metal contacts (Ag, Ni, and Au) in hydrogen environment is studied. In order to get highest relative response of all devices to hydrogen gas, the effective barrier height has been compared and analyzed.

3.2 EXPERIMENTAL SETUP

TiO_2 nanoplates have been deposited on p-Si (100) substrate using RF magnetron sputtering system. TiO_2 target (99.999% purity) is used for the deposition in presence of argon gas (sputter gas) with 100W RF power. Substrate temperature and substrate to target distance are kept at 350˚C and 5cm, respectively. The deposition has been carried out for 2 hours at 8×10^{-3} mbar chamber pressure with Ar flow of 45 sccm. The thickness of TiO_2 nanoplates is ~300nm, which is measured by Dektak XT Profilometer. Structural analysis is performed by X-ray diffraction (XRD) and surface morphology is characterized by Field-effect scanning electron microscope (FESEM). Metal (Al, Ag, Ni, and Au) electrodes of 0.5161mm² area have been deposited on TiO_2 nanoplates using physical mask with the help of thermal evaporation system. The schematic diagram of device based on M/TiO_2 is shown in Figure 3.1.

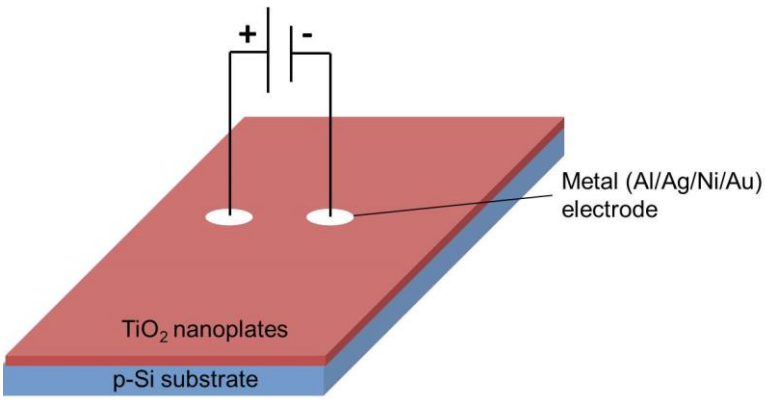

Figure 3.1: Schematic diagram of M/TiO_2 device

The distance between electrodes is around 500 µm in all metals. Electrical and gas sensing characterization of all devices is carried out in 1% hydrogen in pure Ar as well as in air by using Keithley 4200 SCS. Hydrogen gas sensing measurements are performed by applying 1 µA constant current at different temperatures ranging from room temperature (RT) to 175˚C.

3.3 STRUCTURAL PROPERTIES OF TiO_2 NANOPLATES

Anatase phase of TiO_2 is confirmed by XRD and shown in Figure 3.2. Peaks observed at 25.22°, 37.66°, 38.50°, 48.04°, 53.8°, 55.17°, 62.71°, 70.38° , and 75.33° angle are identified as A(101), R(101), A(004), A(200), A(105), R(211), R(002), R(301), and A(215) phase of anatase and rutile

orientation of TiO_2 [Gouma *et al.*, 2001]. From the XRD pattern, anatase-dominated anatase/rutile mixed-phase of TiO_2 is observed.

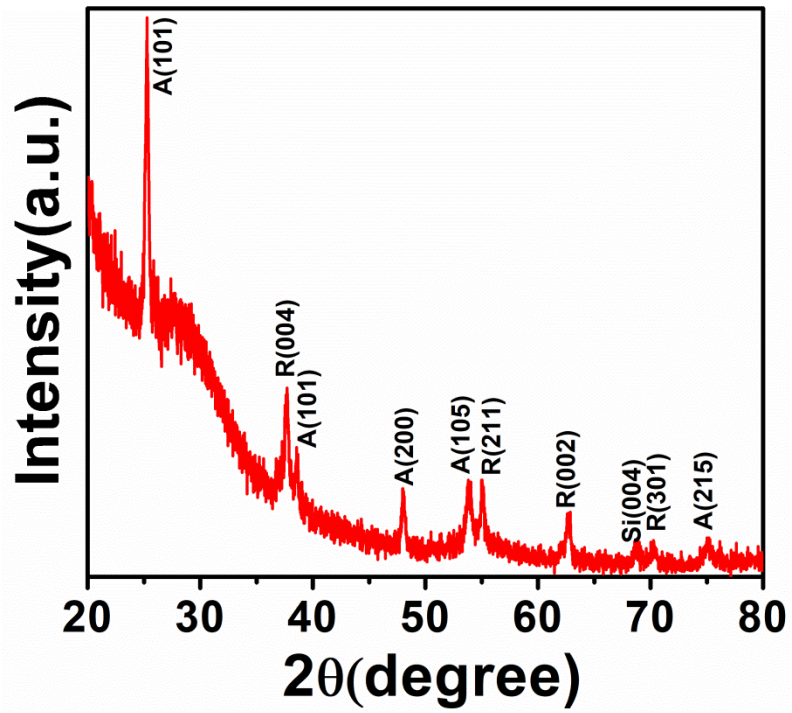

Figure 3.2: XRD spectra of TiO_2 nanoplates

3.4 SURFACE MORPHOLOGY OF TiO_2 NANOPLATES

Surface morphology of TiO_2 can be seen using FESEM and shown in Figure 3.3 (a-b) with top and tilted view. TiO_2 has been deposited in the form of nanoplates with uniform distribution on the substrate.

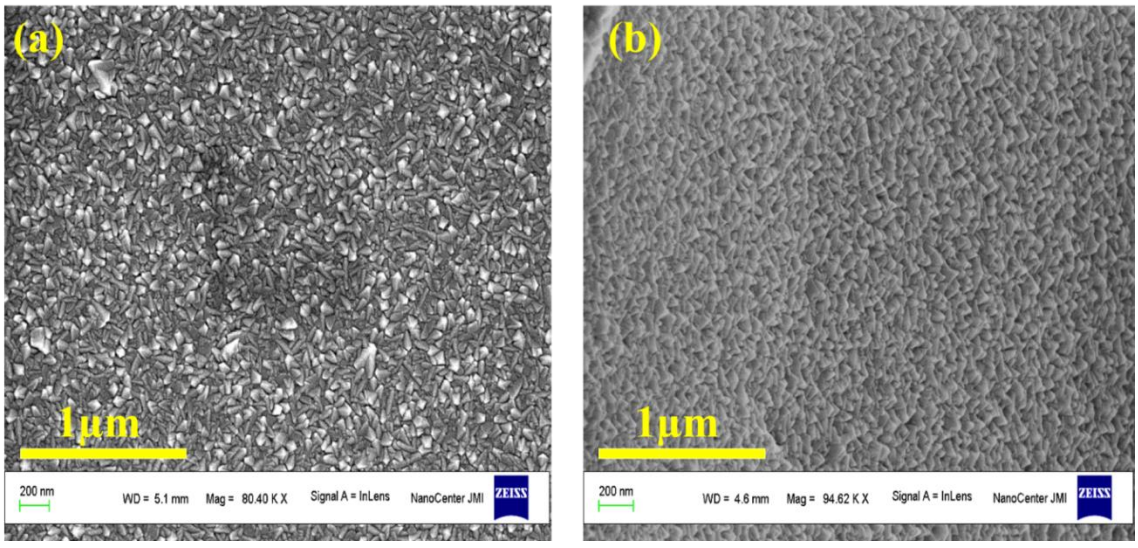

Figure 3.3: FESEM images of TiO_2 nanoplates (a) Top view and (b) Tilted view

3.5 ELECTRICAL CHARACTERIZATION OF M/TiO_2 NANOPLATES

Current-Voltage (*I-V*) characteristics are shown in Figure 3.4 (a-b) which have been carried out in air as well as 1% hydrogen atmosphere (Al/TiO_2, Ag/TiO_2, Ni/TiO_2, and Au/TiO_2) at 175˚C. The interface between Al/TiO_2 nanoplates shows Ohmic behavior and current enhances in the hydrogen environment.

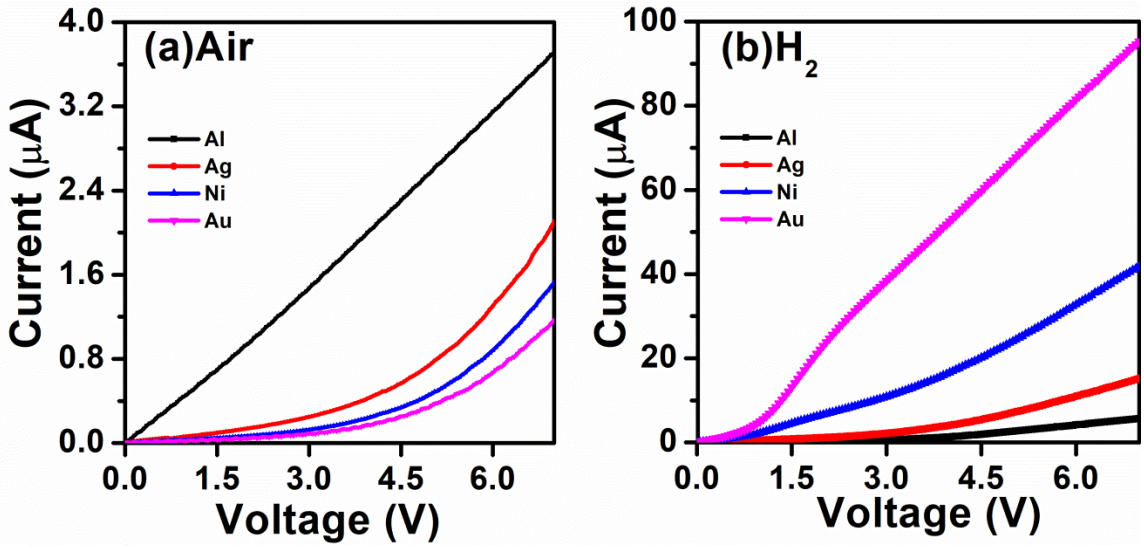

Figure 3.4: Current-Voltage (*I-V*) characteristics of Au/TiO_2, Al/TiO_2, Ag/TiO_2, Ni/TiO_2 in (a) air and (b)1% hydrogen at 175° C

It can also be observed that the effective barrier height (ϕ_B) decreases in hydrogen environment, which leads to increase in current, depending upon the metal work function (Ag<Ni<Au). When hydrogen molecules are exposed to the metal contact, it dissociates into hydrogen atoms. These dissociated hydrogen atoms create dipole layer at the interface of M/TiO_2 and generate an electric field at the junction. Therefore, it decreases the effective barrier height as well as metal work function [Ranwa *et al.,* 2015]. Temperature dependent *I–V* characterization has been carried out to M/TiO_2 devices in air and hydrogen environment from RT to 175˚C. Assuming that the current-transport mechanism is specified by Bardeen model [23], the current density is given by:

$$J = J_r \exp\left(\frac{\beta\sqrt{V_r}}{kT}\right) \tag{3.1}$$

where J_r represents the reverse saturation current density, V_r is the reverse voltage, β is interface related parameter, k is the Boltzmann constant; and T is absolute temperature. J_r can be related to barrier height ($\boldsymbol{\phi_B}$) as shown in the following equation:

$$J_r = A^* T^2 \exp\left(\frac{-q\phi_B}{kT}\right) \tag{3.2}$$

where A^* is defined as the Richardson constant of Si. The semi-logarithmic plot with exponential fitting is shown in Figure 3.5.

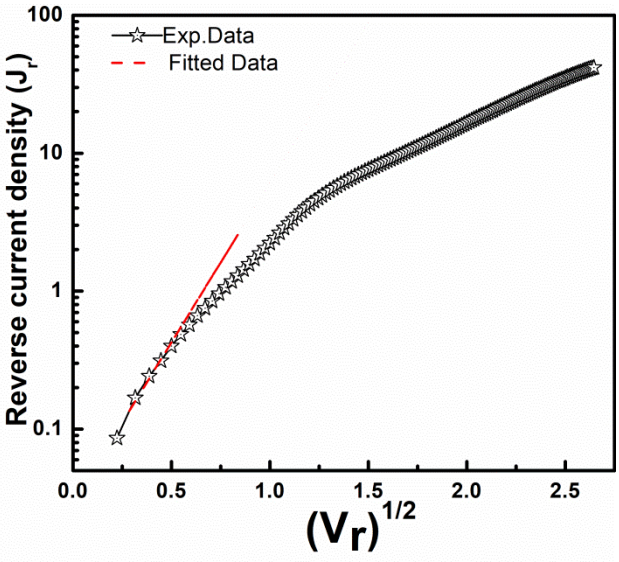

Figure 3.5: Current density versus square root of reverse voltage for Au/TiO_2 in hydrogen at 175˚C

The reverse barrier height of M/TiO_2 devices is given by Eq. (3.3).

$$J = a\exp\left(b\sqrt{V_r}\right) \tag{3.3}$$

where a is defined as J_r which is used to calculate the reverse Schottky barrier height of M/TiO_2. Table 3.1 shows the Schottky barrier height for Au/TiO_2, Ag/TiO_2, and Ni/TiO_2 by using the fitting similar to the one used in Figure 3.5. The change in barrier height from air to hydrogen environment with temperature is shown in Figure 3.6.

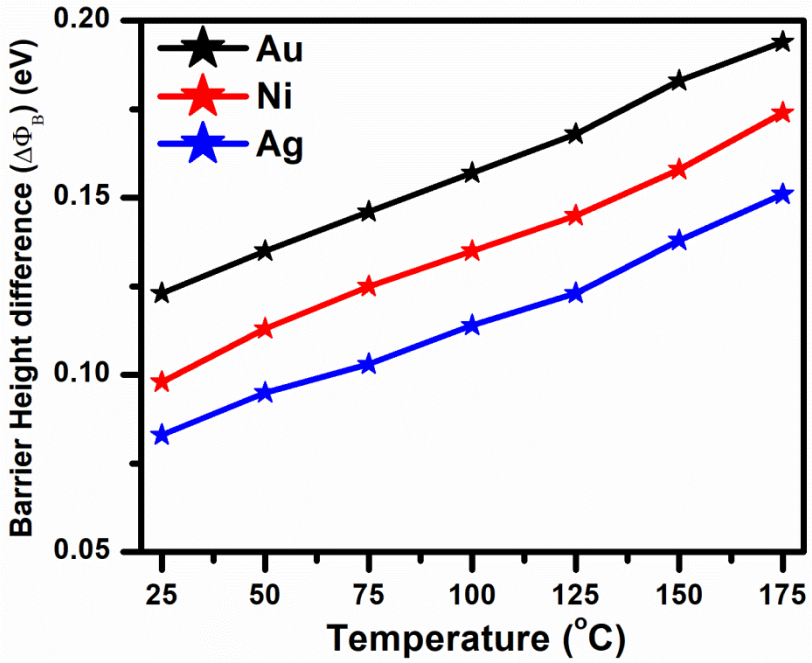

Figure 3.6: Temperature dependent barrier height modulation in air to hydrogen atmosphere

The effective barrier height ($\Delta\phi_B$) is increased as their rise in temperature for all samples. However, Ag electrode shows a small reduction in barrier height (0.15 eV) as compared to Ni (0.17 eV) and Au (0.19 eV) electrodes at 175˚C.

Table 3.1: Calculated Schottky barrier height and effective barrier height of Au/TiO_2, Ag/TiO_2, and Ni/TiO_2 in air and 1% hydrogen atmosphere at different temperature

T(°C)	In Air			In H_2			Effective barrier height		
	ϕ_{Au} (eV)	ϕ_{Ni} (eV)	ϕ_{Ag} (eV)	ϕ_{Au} (eV)	ϕ_{Ni} (eV)	ϕ_{Ag} (eV)	$\Delta\phi_{Au}$ (eV)	$\Delta\phi_{Ni}$ (eV)	$\Delta\phi_{Ag}$ (eV)
25	0.831	0.748	0.718	0.708	0.665	0.62	0.123	0.098	0.083
50	0.828	0.722	0.699	0.692	0.627	0.586	0.135	0.113	0.095
75	0.822	0.72	0.688	0.676	0.617	0.563	0.146	0.125	0.103
100	0.817	0.718	0.684	0.66	0.592	0.553	0.157	0.135	0.114
125	0.813	0.707	0.68	0.645	0.584	0.536	0.168	0.145	0.123
150	0.811	0.702	0.674	0.628	0.564	0.516	0.183	0.158	0.138
175	0.8	0.696	0.662	0.606	0.545	0.488	0.194	0.174	0.151

Therefore, effective barrier height as well as metal work function of devices decrease which increases the sensor's relative response towards hydrogen gas.

3.6 HYDROGEN GAS SENSING STUDIES OF TiO_2 NANOPLATES

Figure 3.7 depicts the relative response curve with respect to time of Al/TiO_2, Ag/TiO_2, Ni/TiO_2, and Au/TiO_2 sensor at 175°C to 1% hydrogen.

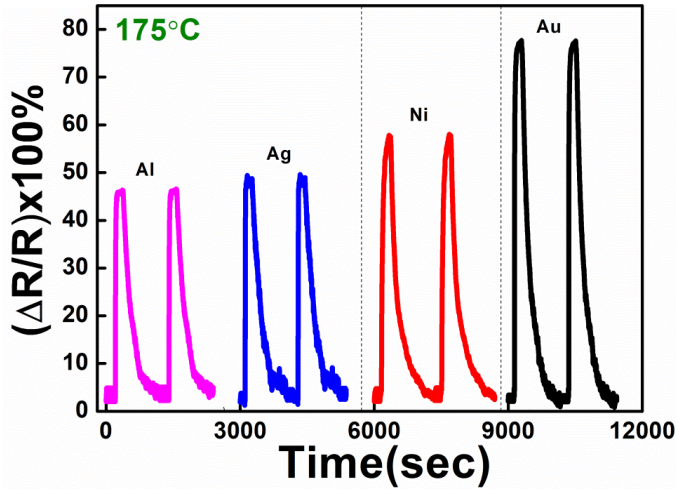

Figure 3.7: Relative response curve of Al/TiO_2, Ag/TiO_2, Ni/TiO_2, and Au/TiO_2 at 175°C to 1% hydrogen

It can be observed that Au/TiO_2 has changed the resistance more than other metal electrodes at same operating temperature. The devices based on Au/TiO_2 observe maximum sensing response as compared to Ni/TiO_2, which is attributed to more solubility of hydrogen at the interface of Au/TiO_2. Than Ni/TiO_2 Moreover, hydrogen sensing response for Ag/TiO_2 decreases with small reduction in Schottky barrier height. Large reduction in barrier height at M/TiO_2 devices (except Al) is attributed to more adsorption of oxygen ions at the operating

temperature which leads to high relative response towards hydrogen. On the other hand, Al/TiO_2 shows ohmic behavior, due to which sensing response comes only from surface reaction.

In Figure 3.8 (a-d), temperature dependent hydrogen gas sensing curve is shown for all M/TiO_2 sensors. Sensing response of each device increases with increasing temperature, which is due to high diffusion rate leading to large interaction of hydrogen over TiO_2 nanoplates.

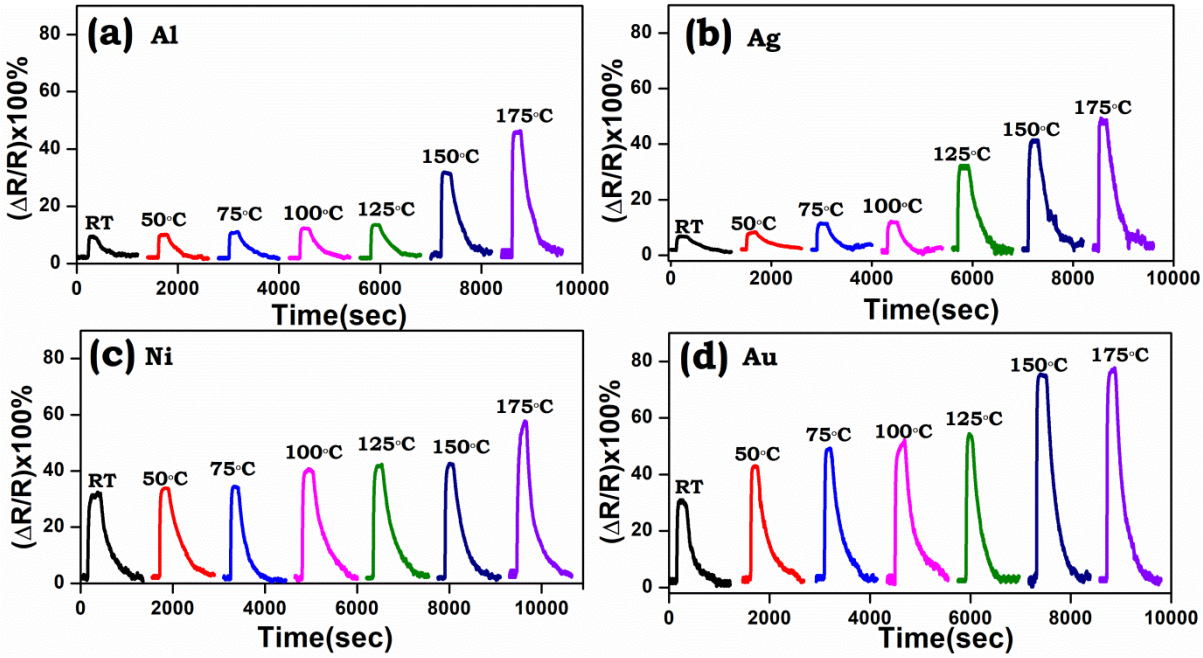

Figure 3.8: Temperature dependent hydrogen sensing curves of (a) Al/TiO_2 (b) Ag/TiO_2 (c) Ni/TiO_2 and (d) Au/TiO_2

Figure 3.9 depicts the decrease in base resistance with increasing temperature, which is a well-known fundamental property of semiconductors.

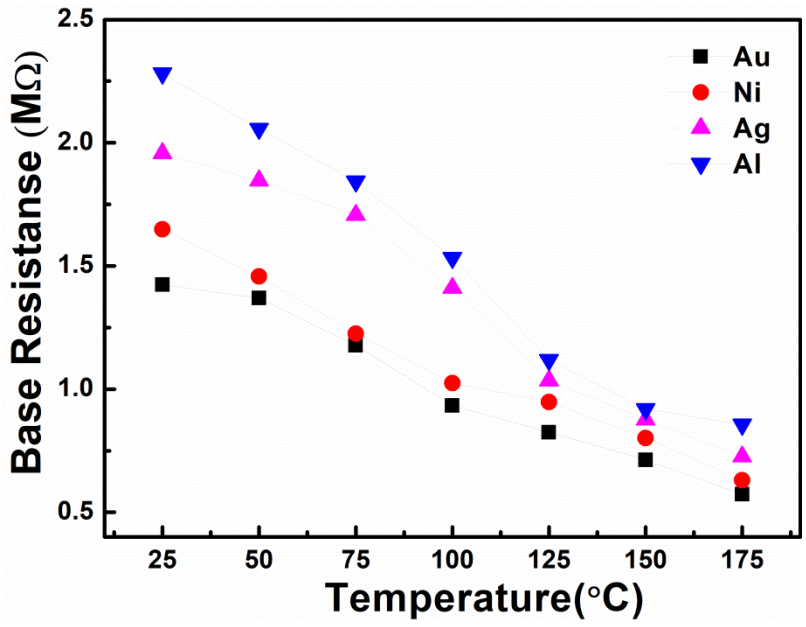

Figure 3.9: Base resistance as a function of temperature at fixed 1 μA current

Relative response enhances via adsorption/desorption of reactive gases at the junction of metal and TiO_2 nanoplates. Noble metal electrodes also act as a catalyst for hydrogen adsorption. When hydrogen molecules diffuse into metal electrodes, change in barrier height of M/TiO_2 junction is observed. This leads to enhance the sensing response by reduction of metal work-function with high temperature. Hydrogen gas sensing on TiO_2 nanoplates has been characterized in terms of relative response, response time, and recovery time with respect to operating temperature (RT to 175˚C). Response and recovery time can be calculated from exponential change in resistance curves [Ranwa *et al.*, 2015] as given below:

$$R_{res} = R_{\circ} + A \exp(\frac{-t}{\tau_r}) \tag{3.4}$$

$$R_{rec} = R_1 + B \exp(\frac{t}{\tau_d}) \tag{3.5}$$

where A and B are the scaling constants, τ_d is the response time and τ_r is the recovery time. Response and recovery time of all sensors at different operating temperature (RT to 175˚C) have been calculated from experimental data by fitting, according to the Eqs. (3.4) and (3.5). Figure 3.10 (a) and (b) represent the change in response time and recovery time with increasing temperature.

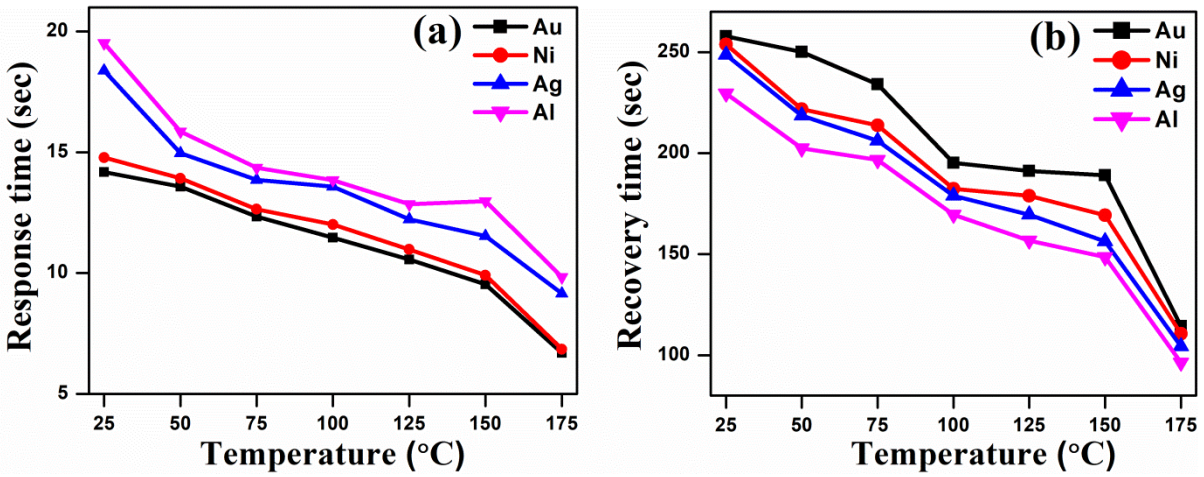

Figure 3.10: Variation of (a) response time and (b) recovery time with temperature

It can be observed that response time of the sensors reduces with increasing temperature. The fast response and moderate recovery times is calculated as 7 and 114 sec respectively, for Au electrode. This is mainly caused by the fast desorption of oxygen ions at TiO_2 surface, which reduces the barrier height. A large change in recovery time reveals that more hydrogen reacts with these oxygen ions. Gas sensor's sensing response (S) is defined as the relative change in resistance of TiO_2 sensor in hydrogen gas with respect to air, which is expressed as Eq. (3.6) [Lupan *et al.*, 2010]

$$S = \left(\frac{R_a - R_g}{R_a}\right) \times 100\% \tag{3.6}$$

where $\Delta R = (R_a - R_g)$, R_a is the resistance in air and R_g is the resistance in hydrogen gas. Figure 3.11 shows the relative response of M/TiO_2 devices with increasing operating temperature.

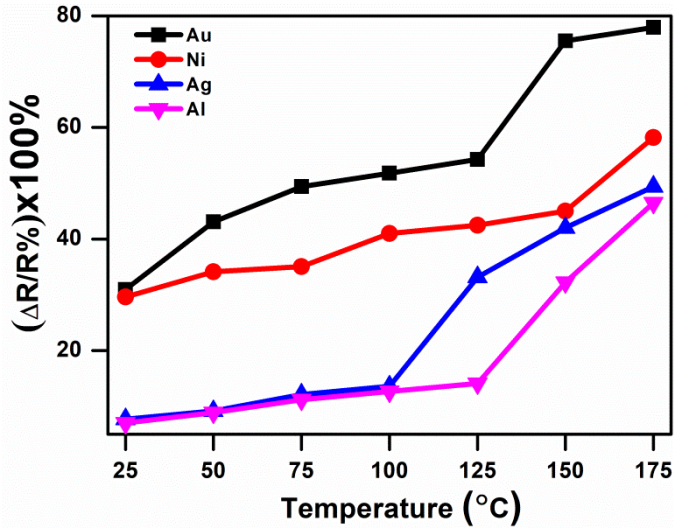

Figure 3.11: Relative response of M/TiO_2 structure with temperature

Relative response of sensor increases with increasing temperature which is due to the enhanced diffusion rate of hydrogen gas at the interface of metal and TiO_2 nanoplates and reduction in work function of the metal.

3.7 PROPOSED HYDROGEN GAS SENSING MECHANISM FOR M/TiO2 NANOPLATES

Hydrogen gas sensing mechanism for TiO_2 can be explained by alteration of electron depletion layer on TiO_2 surface. The oxygen molecules are chemisorbed on TiO_2 surface and the electrons are ejected from conduction band of TiO_2 nanoplates. Then, oxygen molecules convert into oxygen ions due to high electronegative nature of oxygen, as shown in Figure 3.12 (a). Therefore, an electron depletion region is formed on surface, resulting in net reduction of electron density, which subsequently enhances the resistance of TiO_2. When hydrogen gas is exposed to the sensor, chemisorbed oxygen is reacting with the hydrogen molecules. This leads to change in depletion region as shown in Figure 3.12 (b). Therefore, free electrons come back to the conduction band, and thus decreasing resistance of the sensor. However, once hydrogen is removed from the sensing chamber, the depletion region will form again, and further increasing the resistance. The major factors that influence the sensor's characteristics are hydrogen concentration, operating temperature, and shapes of nanostructures. Operating temperature also plays a big role in hydrogen sensing, which boosts the diffusivity of hydrogen atoms onto the TiO_2 surface, consequently enhancing the sensitivity. However, high operating temperature is undesirable due to high power consumption and safety issues.

Hence, it is highly required to use the metals (Ag, Ni and Au) to achieve better sensitivity due to their catalytic properties. This increases the interaction between TiO_2 and hydrogen molecules, which leads to reduction in the operating temperature. Here, all these metals exhibit Schottky behavior except Al/TiO_2 nanoplates, resulting in large reduction in barrier height as well as increased sensitivity. Figure 3.12 (c-h**)** shows the band diagram of Ag/TiO_2, Ni/TiO_2, and Au/TiO_2 in air and hydrogen environment. Here, large change in effective barrier height is observed for Au/TiO_2 junction. Moreover, highest relative response is occurs for Au (77%). However, the order of relative response for other electrodes has been found to be: Al (46%) < Ag (49%) < Ni (58%) < Au (77%).

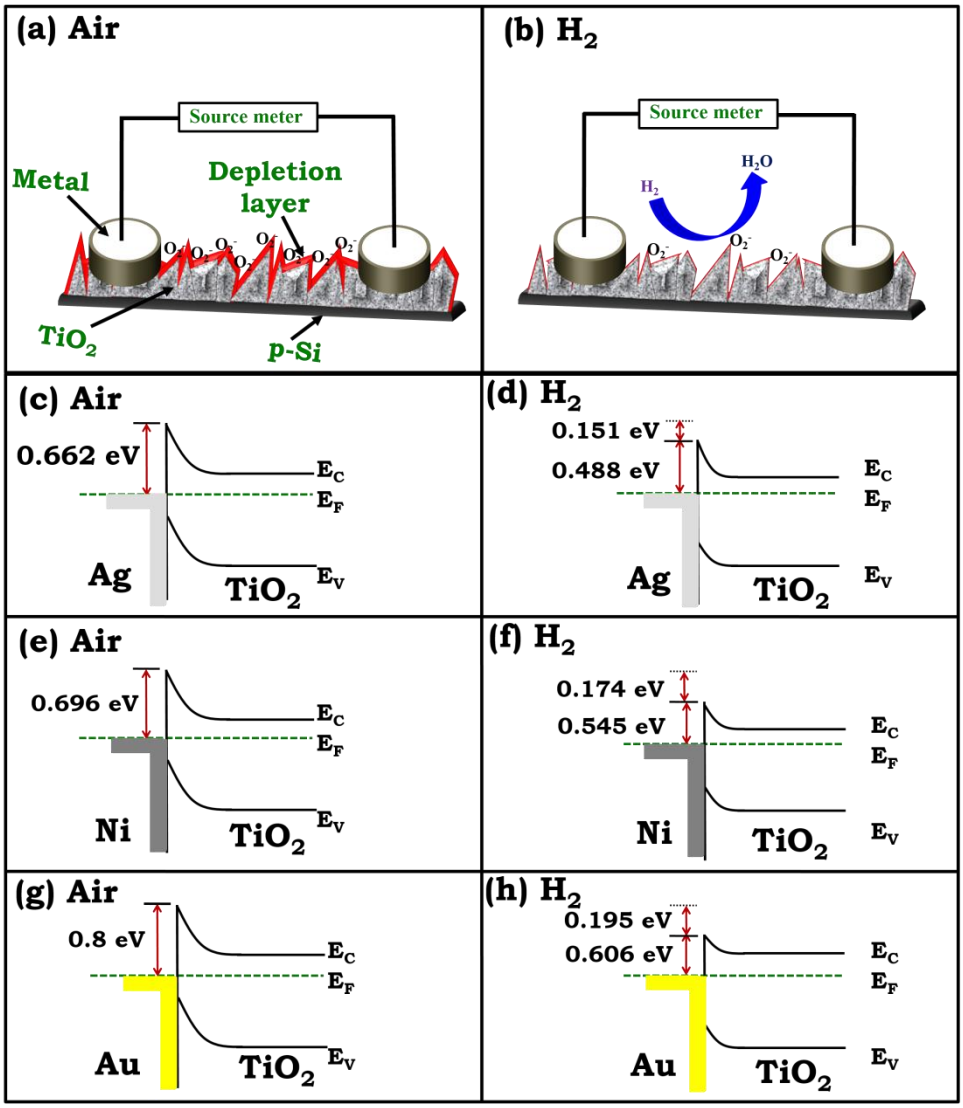

Figure 3.12: Schematic illustration of hydrogen sensing mechanism in (a-b); Energy band diagram of M/TiO_2 in (c), (e) and (g) for air and (d), (f) and (h) for hydrogen

3.8 CONCLUSION

In conclusion of this chapter, TiO_2 nanoplates of anatase dominated phase have been deposited on p-Si substrate by RF magnetron sputtering. Schottky barrier height between metal and semiconductor is modulated by different metal electrodes (Ag, Ni, and Au) on TiO_2 nanoplates, which enhances the sensing response towards hydrogen gas. The effective barrier height is calculated as ~0.15 eV for Ag, ~0.17 eV for Ni, and ~0.19 eV for Au electrodes at 175˚C. Highest effective barrier height is observed for Au electrode which corresponds to large change in relative response ~77%. For Au electrode, fast response and moderate recovery times are observed as ~7 and 114 sec, respectively. This proves that the Schottky barrier height strongly affects the relative response of the sensor.

4

Effect of Ni Doping into ZnO Nanostructures for Structural, Morphological, Electrical, and Gas Sensing Properties

In this chapter, the impact of Ni doping into ZnO nanostructures on structural, morphological, electrical, and hydrogen gas sensing performance will be described. Different concentration of Ni is doped into ZnO to detect extremely low concentration (1 ppm) of hydrogen at mild operating temperature of 75°C. Ni doping exceptionally increases the sensing response and decrease the operating temperature of the sensor than undoped ZnO. The main role of the Ni-doping is to produce more active sites for chemisorbed oxygen on the sensor's surface and, correspondingly, upgrade the sensing response. In addition, the gas sensing mechanism will be discussed in the end of this chapter.

4.1 INTRODUCTION

Doping of transition metal element into MO_x is one of the eminent factors which improve the sensing response of MO_x sensor. Transition metals like Ni, Co, Fe and Cu have been mostly used as dopants into MO_x [Zhang *et al.*, 2017; Maswanganye *et al.*, 2017; Bai *et al.*, 2014; Gong *et al.*, 2006]. Dopants not only modify the resistance but also increase the sensing response of MO_x sensor. These metal dopants also play a vital role in decreasing the operating temperature of the gas sensor, and improving selectivity, stability, and response time for target gas molecules. It has been noticed that the surface morphology of MO_x changes after doping the metal elements into it. The grain size of doped MO_x nanostructures becomes smaller as compared to pure MO_x nanostructures, which is due to further restrictions of movement of crystallites during the interaction of boundaries between the dopant and the host material [Maciel *et al.*, 2003]. Therefore, the growth of crystal stops because of introduction of dopant element. Gas sensing response can be enhanced by using small-sized particles having high surface area; resulting in the enhancement of large number of chemisorbed oxygen ions and increased barrier height. Keeping in mind this motivation, ZnO, has been used as a host material in this work because it is one of the most favorable MO_x [Kobrinsky *et al.*, 2008; Zhu *et al.*, 2005]. Performance of the ZnO-based gas sensors is largely affected by the dimension of nanostructures of a sensing layer and operating temperature [Ranwa *et al.*, 2014]. Li *et al.* [Li *et al., 2014*], grew TiO_2 nanotubes doped with 8% Ni which shows a maximum sensing response of ~24% and ~65% to 2% hydrogen at RT and 200°C, respectively. Authors in [Yang *et al.*, 2015] investigated the 2 at% Cd doped ZnO nanorods grown by hydrothermal method that was able to sense 500 ppm of H_2 gas at operating temperature ranging from 50°C to 100°C. Liu *et al.*, reported Mg-doped ZnO thin films exhibiting gas sensing response (R_a/R_g) for about 1.7 to 5 ppm H_2 at 150°C [Liu *et al.*, 2011]. Sett *et al.* [Sett *et al.*, 2017], synthesized Co-doped ZnO nanorods and then characterized them within the range of 1000 to 3000 ppm H_2. The sensing response was outstanding for ZnO with 8 mol% of Co, and showed ~3 times better sensitivity for 3000 ppm of H_2 gas at 300°C as compared to undoped ZnO. Shen *et al.* [Shen *et al.*, 2009] synthesized undoped and Pd-doped SnO_2 nanowires and exhibited a reversible response to H_2 gas at operating temperatures between RT and 300°C. Sensor based on 2 wt% Pd doped SnO_2 nanowires revealed an excellent response of ~253 to 1000 ppm of H_2 gas at 100°C.

This chapter demonstrates highly sensitive Ni-doped ZnO sensor which is able to detect extremely low concentration of hydrogen at mild operating temperature (75°C). The operating

temperature for this sensor is much lower than previous reports in literature (>150°C). ZnO has been doped with 0%, 2%, 4% and 6% of Ni, using RF magnetron sputtering system and then gas sensing response has been carried out for hydrogen gas sensing response with respect to the operating temperature (RT to 150°C) .

4.2 EXPERIMENTAL SETUP

Undoped and Ni-doped ZnO nanostructures have been grown on p-Si (100) substrate by using an RF sputtering system. A ZnO target (99.99% purity) is utilized for the deposition under Ar gas environment. Ni chips (3×3 mm^2) were also attached on ZnO target to get the desired doping concentration of Ni (2, 4, and 6%) into the ZnO lattice, as shown in Figure 4.1. Sputtering parameters such as substrate temperature, RF power, and substrate to target distance were fixed at 600˚C, 50W and 5cm, respectively. The deposition has been done in 2 h at 1.5×10^{-2} mbar chamber pressure with an Ar flow of 25 sccm. Surface morphology and structural analyses of the undoped and Ni-doped ZnO were carried out using field emission scanning electron microscopy (FESEM, JSM 7100F, Jeol) and an X-ray diffractometer (XRD, Bruker D8 Advance), respectively. CL studies have been carried out at room temperature using CL spectroscopy apparatus (MONO CL4, Gatan) installed with scanning electron microscope (JSM-7100F, JEOL). Therefore, circular shaped aluminum (Al) electrodes having diameter of 400µm have been fabricated on ZnO-based nanostructures by using thermal evaporation system with the help of shadow mask.

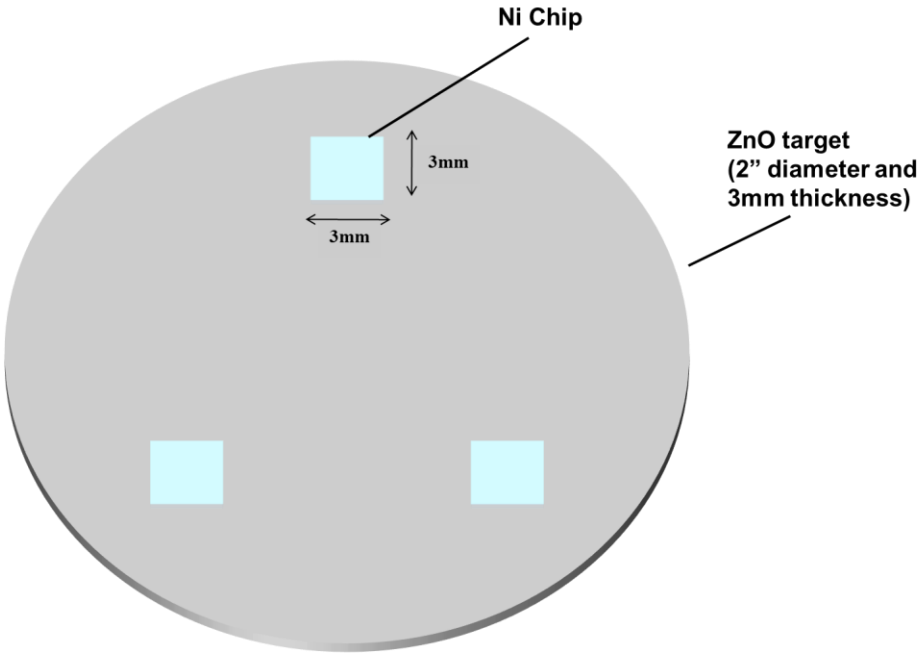

Figure 4.1: Schematic diagram of ZnO target

A gas sensing setup has been used to detect 1% hydrogen in pure argon environment using semiconductor characterization system (SCS- 4200, Keithley). 10% RH in sensing chamber has been maintained during gas sensing measurements. A constant operating voltage (3V) is applied to the sensor during the measurement, and sensor's resistance response curve has been taken out via *I-V* characteristics. Thereafter, hydrogen sensing measurements have been performed at the operating temperature ranging from RT to 150˚C. For ppm level of hydrogen detection, pre-calibrated volume of 1% hydrogen gas in Ar is introduced into sensing chamber by using gas tight syringe.

4.3 STRUCTURAL CHARACTERIZATION

Figure 4.2 (a-d) shows the XRD pattern of undoped and Ni-doped ZnO nanostructures deposited on p-Si (100) substrate. XRD pattern of undoped ZnO reveals a strong (002) peak related to the hexagonal wurtzite structure along with highly orientated c-axis [Zhang *et al.,* 2017].

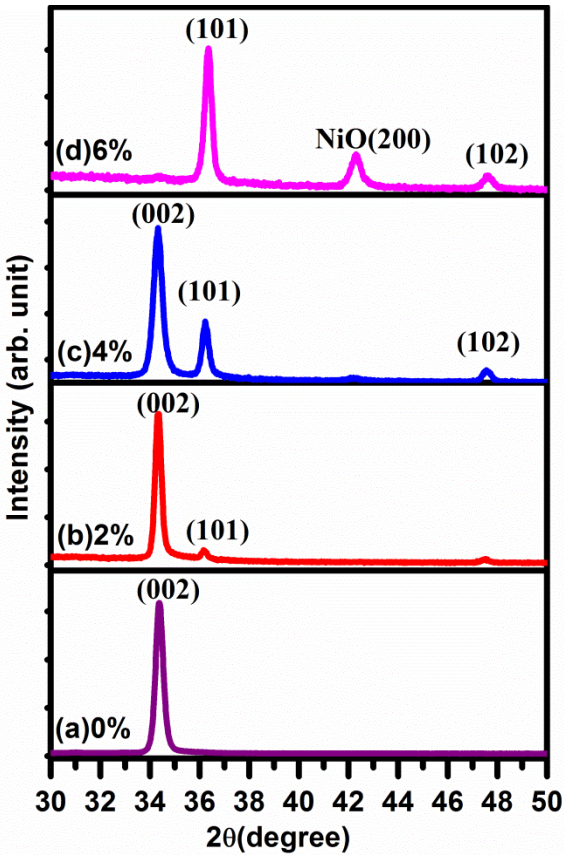

Figure: 4.2 XRD pattern of (a) undoped, (b) 2% Ni- doped, (c) 4% Ni- doped and (d) 6% Ni- doped ZnO nanostructures

Other planes such as (101) and (102) have been observed with increased peak intensity as doping concentration increases from 2 to 4% Ni into ZnO. No other peaks are found corresponding to NiO or Ni, which depict the substitution of Zn^{+2} ions (0.074 nm) by Ni^{+2} ions (0.069 nm) [Bouaoud *et al.,* 2013]. Upon further addition of Ni doping to 6%, (002) peak of ZnO vanishes and a small peak can be seen at $2\theta = 42.33^{o}$ corresponding to NiO which indicates the existence of NiO phase with ZnO [Long *et al.,* 2014]. The removal of (002) peak of 6% Ni is caused by lattice distortion and degraded crystallinity of ZnO nanostructures along the c- axis. This degraded crystallinity might be due to the different ionic radii of Zn and Ni ions which generates stress and creates crystal deformation. Tsay *et al.* [Tsay *et al.,* 2012] has investigated that 5% Ga doped ZnO did not show the (002) peak in XRD spectra, thus indicating the degraded crystallinity of Ga doped ZnO thin films.

4.4 FILM MORPHOLOGY

Effect of Ni doping on morphology of ZnO has been investigated by using FESEM. Figure 4.3 (a-h) depicts top view as well as cross sectional view of undoped (2, 4, and 6%), and Ni- doped ZnO nanostructures, respectively.

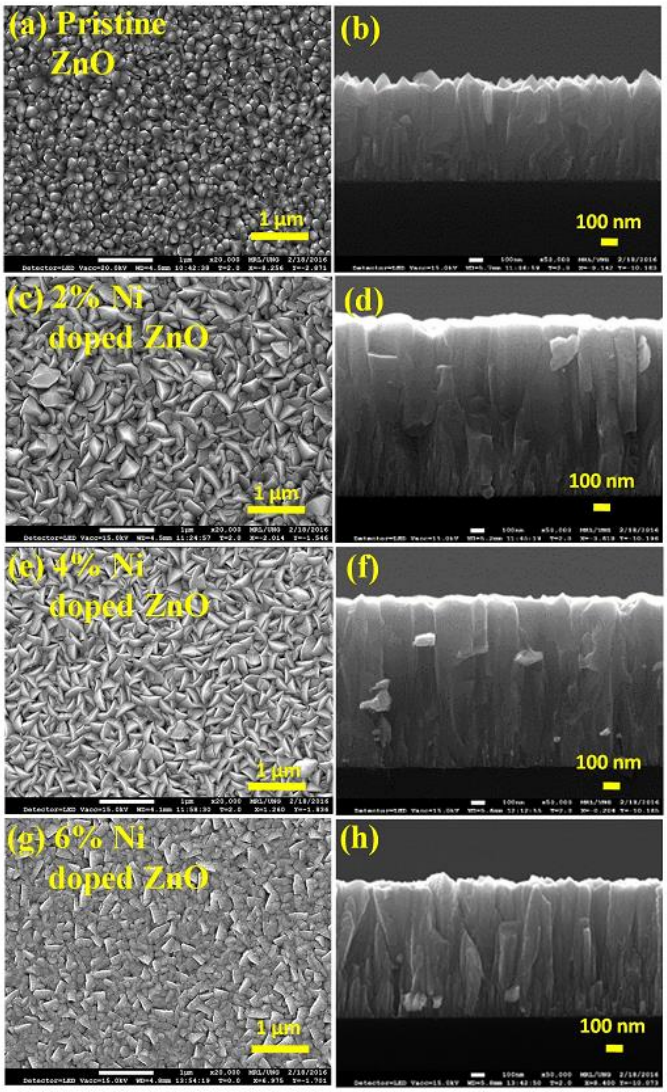

Figure 4.3: (a-h) Top view and cross sectional view of FESEM images for (a-b) undoped, (c-d) 2% Ni- doped, (e-f) 4% Ni- doped and (g-h) 6% Ni- doped ZnO nanostructures

Undoped ZnO nanostructures represent columnar structure along the conical tips of highly dense packed ZnO nanorods uniformly deposited throughout the substrate as shown in Figure 4.3 (a). However, the surface morphology of ZnO nanostructures has been transformed with increasing concentration of Ni. When Ni dopant is introduced into ZnO, conical tips of ZnO nanostructures transform into nanoplates (Figure 4.3 (c-e)). Here, XRD spectra also prove the change in the preferred orientation of the deposited film induced by Ni-doping. The columnar structure with nanoplates morphology is present in 2% and 4% Ni doped ZnO; while for the 6% Ni, columnar structure with rectangular surface can be observed in FESEM images. The amounts of Ni doping (2±0.1, 4±0.1, and 6±0.1 %) in ZnO have been confirmed by EDX quantitative analysis which can be seen in Figure 4.4.

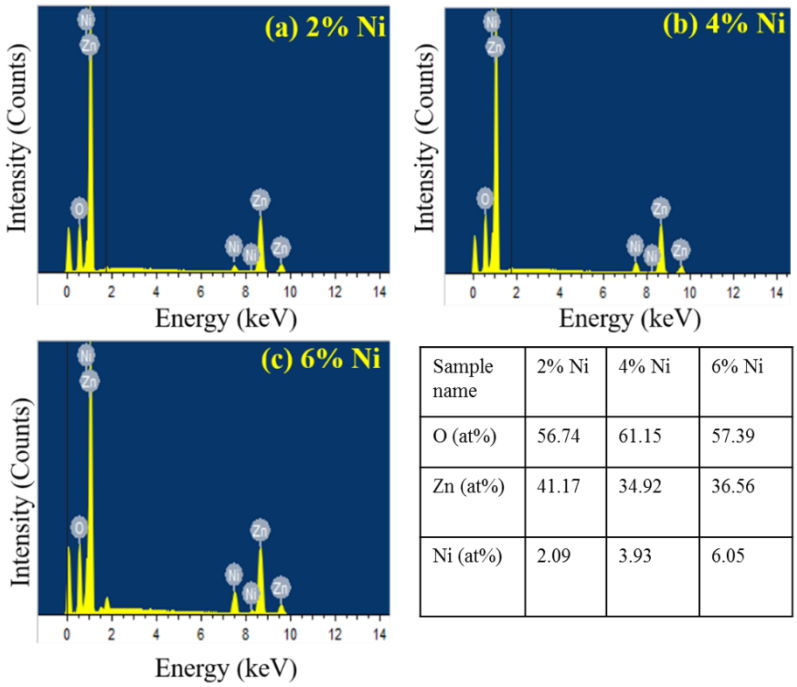

Sample name	2% Ni	4% Ni	6% Ni
O (at%)	56.74	61.15	57.39
Zn (at%)	41.17	34.92	36.56
Ni (at%)	2.09	3.93	6.05

Figure 4.4: (a-c) EDX spectra of 2%, 4%, and 6% Ni -doped ZnO nanostructures, respectively

4.5 OPTICAL PROPERTIES

CL characterization of undoped and 4% Ni-doped ZnO nanostructures at room temperature reveals a clear picture about crystallinity and structural defects in Figure 4.5.

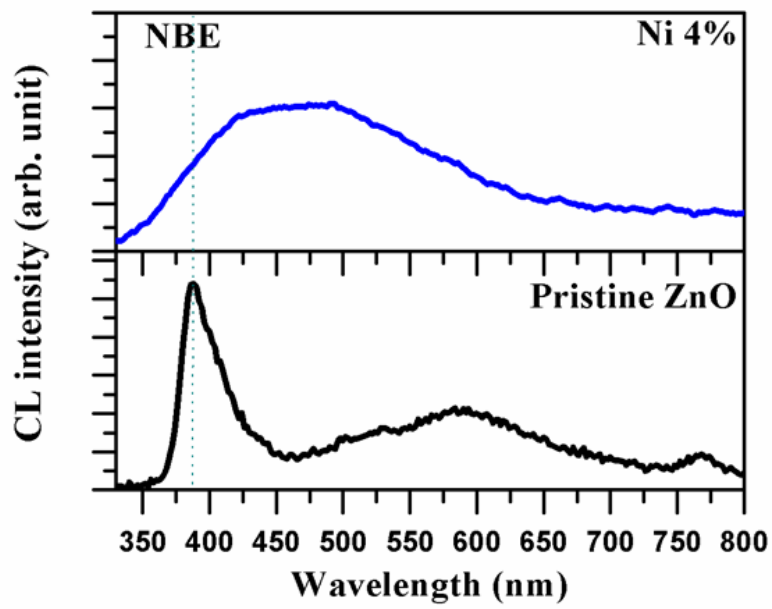

Figure 4.5: CL spectra of undoped and 4% Ni -doped ZnO nanostructures at RT

Undoped ZnO reveals a strong NBE peak at ~ 385 nm which confirms the crystalline growth of ZnO nanostructures. Moreover, 4% Ni doped ZnO nanostructures suggests the presence of broad peak at 400-700 nm with respect to undoped ZnO. This wide band emission region shows the presence of structural defects like oxygen vacancies (V_o), interstitial defects, and antisite oxygen (O_{zn}) that might have existed in 4% Ni doped ZnO nanostructures [Abbasi *et al.,* 2014].

4.6 ELECTRICAL CHARACTERIZATION

Current conduction mechanism of Ni-doped ZnO nanostructures based sensor has been described using electrical characterization techniques. Figure 4.6 (a) and 4.6 (b-e) represents the schematic diagram of device and their Current-Voltage (*I-V*) characteristics in air and 1% H_2 at 150°C, respectively. Initially, undoped ZnO nanostructure with Al contacts shows ohmic behaviour in air and H_2 gas. Higher current has been observed in presence of hydrogen, attributed to decrease in depletion width of chemisorbed oxygen ions on ZnO nanostructures surface [Ranwa *et al.*, 2015]. On the other hand, 4% Ni- doped ZnO having columnar structure of nanoplates surface revealing rectifying behavior, which also indicates that the current of the Ni-doped ZnO sensor decreases from hundreds of micro ampere to few micro amperes than undoped ZnO. This is caused by the presence of higher barrier height between metal and ZnO as well as between the columnar structures of nanoplates shape in 4% Ni-doped ZnO sample, attributed to large change in resistance in air and hydrogen environment than undoped ZnO.

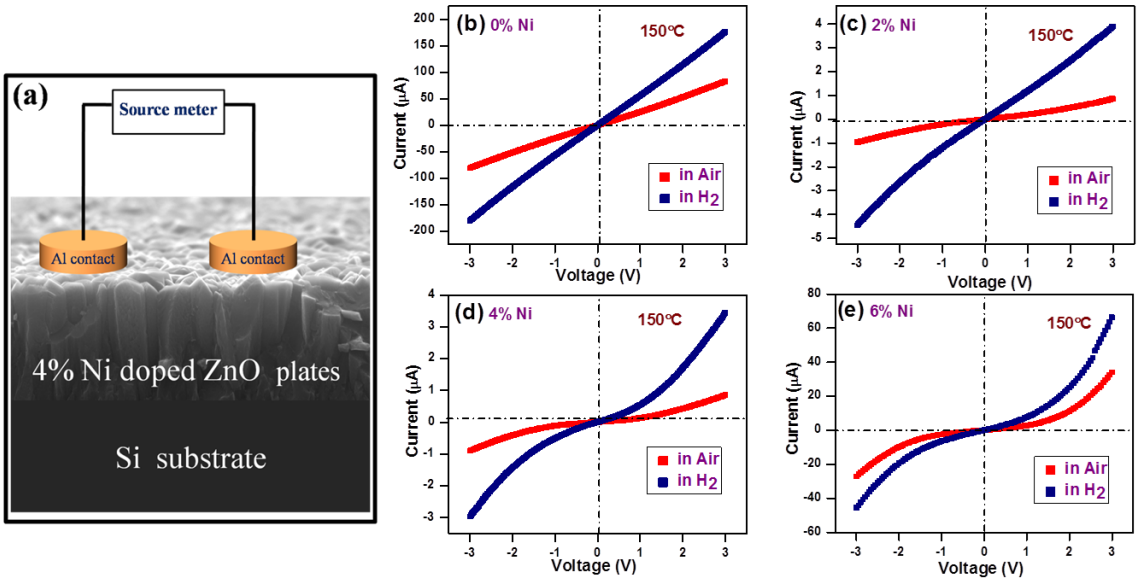

Figure 4.6 (a) Schematic diagram of Sensor device, (b-e) I-V characteristics of undoped, 2% Ni-doped, 4% Ni-doped, and 6% Ni- doped, ZnO nanostructure in presence of air as well as 1% hydrogen at 150°C

It is observed that the sensor current in sensor increases in air in 6% Ni–doped ZnO. The higher current might be due to change in growth direction of ZnO and generation of more defects at higher dopant concentration of Ni. Separation of NiO (p-type) from ZnO (n-type) has been initiated in 4% Ni doped ZnO (clearly seen in XRD spectra), which further became higher in 6% Ni doping. Herein, the *I-V* characteristics of the Ni doped ZnO nanostructures are strongly affected by the ratio of p-n heterojunction to the ZnO barrier. If this ratio is too high, then the relative change in current of sensor will be significantly low because of less reaction between chemisorbed oxygen ions and target gas [Zhiming *et al.*, 2012]. The relative change in current has been maximized at the optimum condition when the ratio of p-n heterojunction to the ZnO barrier is balanced. This ratio was found suitable for 4% Ni. Further adding of Ni dopant upto 6% leads to enhancement in the p-n heterojunction and decrease in the total number of ZnO barriers. Consequently, the p-n heterojunction became highly dominated at higher content of Ni doping, and the current conduction decreases at this amount. Moreover, the *I-V* characterization of 4% Ni doped ZnO is also evident for optimum condition of the ratio of p-n heterojunction to ZnO barrier, and shows large change in ZnO barrier height in presence of air to hydrogen gas than 6% Ni doped ZnO.

4.7 HYDROGEN SENSING MEASUREMENT

In MO_x based gas sensors, gas sensing is basically a surface phenomenon. The key factors like operating temperature, gas concentration, and doping amount strongly influence the sensing response. Relative response of the gas sensor can be calculated by relative change in resistance in air and analyzed gas. Sensor response at 1% for hydrogen has been studied from RT to 150 °C. Figure 4.7 (a-d) shows the relative response of gas sensor for undoped, 2, 4, and 6% Ni- doped ZnO nanostructures. It can be observed that the operating temperature has significant impact on the sensor's response. Relative response of undoped ZnO sensor increases from ~3.5% to 43.4% for 1% H_2 gas when temperature increases from RT to 150 °C. Moreover, there is also a significant improvement in sensor's response for Ni doped films, whereas 4% Ni dopant increases from ~10% to 68.8%, which is approximately ~1.5 times larger than the undoped ZnO. Further enhancement in Ni doping decrease sensor response as compared to undoped ZnO nanostructures based sensor.

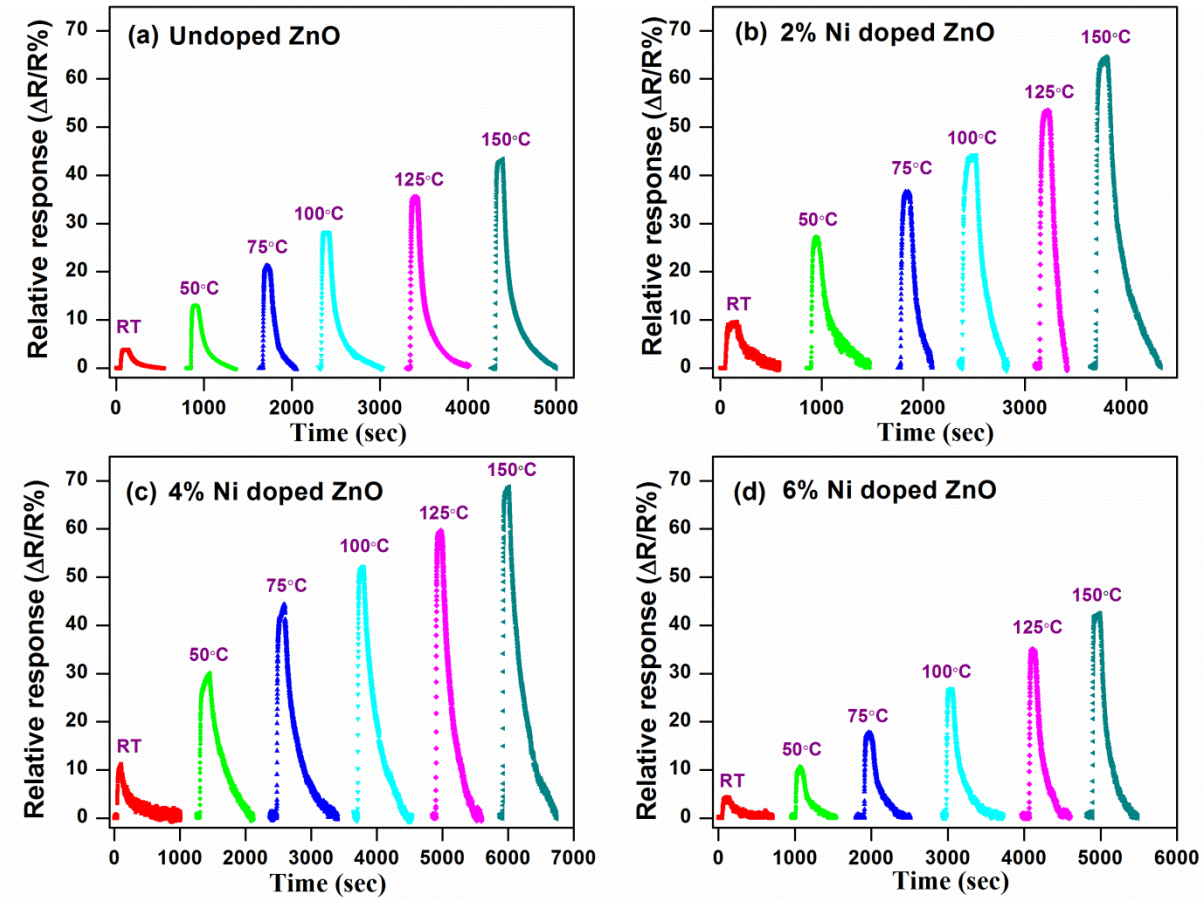

Figure 4.7: Gas sensor relative response for undoped, 2%, 4%, and 6% Ni- doped ZnO nanostructures with increasing operating temperature ranging from RT to 150°C for 1% hydrogen concentration

The comparison of relative response for all sensors at 150°C is shown in Figure 4.8. Maximum relative response ~68.8% has been observed by 4% Ni- doped ZnO nanostructures than undoped ZnO nanostructure (~43.4%). Further addition of Ni doping up to 6% decreases the sensor relative response to ~42.3%, which is almost similar to undoped ZnO nanostructure.

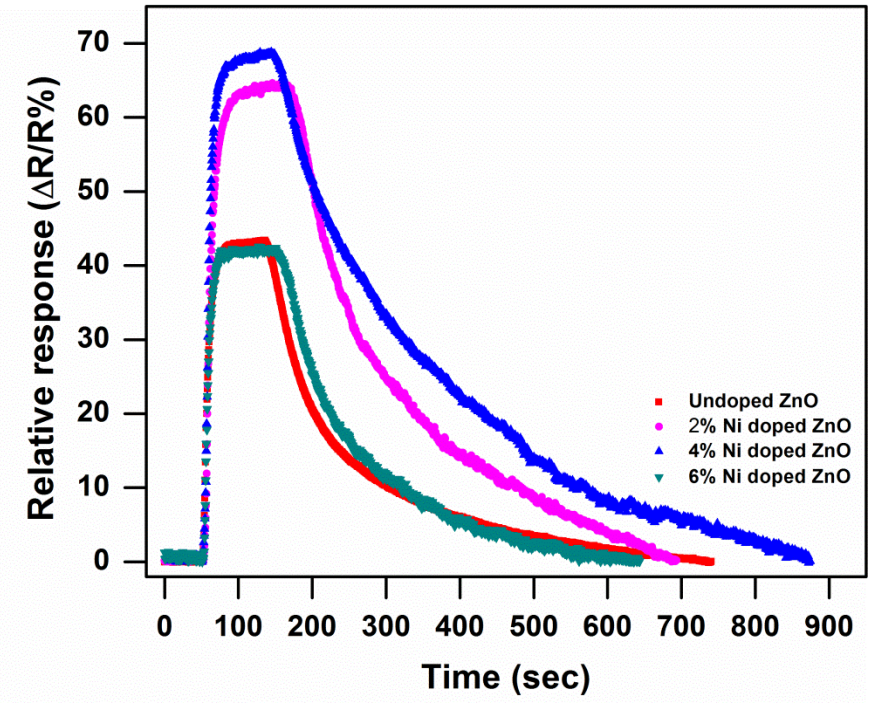

Figure 4.8: Relative response of undoped and Ni- doped ZnO nanostructures based sensor at 150°C

Long-term stability test is also a crucial factor for gas sensors in real market applications [Korotcenkov *et al.,* 2011]. Figure 4.9 shows long-term stability curve for 4% Ni-doped ZnO nanoplates where the sensing measurement has been tested up to 150 days in 1% hydrogen at 150 °C.

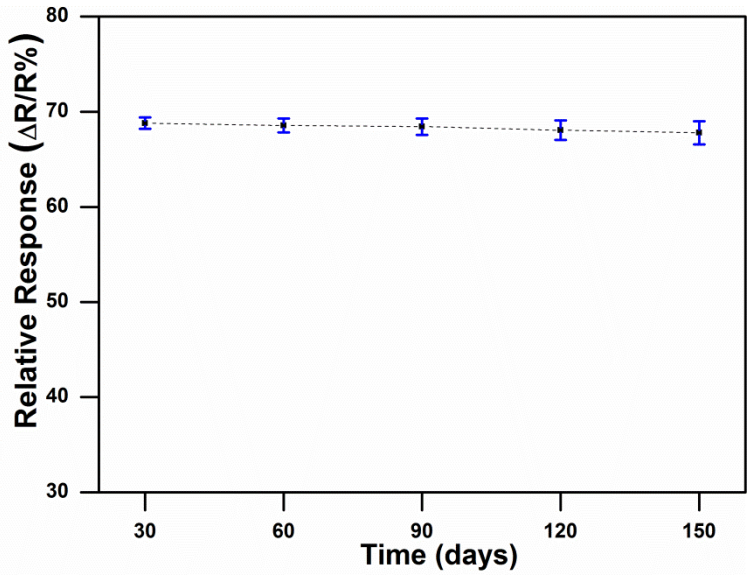

Figure 4.9: Long term stability curve of 4% Ni- doped ZnO nanoplates for 150 days

It has been observed that the relative response is stable with time. The hydrogen gas detection in ppm level is also possible for this sensor at moderate operating temperature. Figure 4.10 shows the relative response of 4% Ni-doped ZnO based sensor with increasing hydrogen concentration from 1ppm to 100 ppm at moderate operating temperature of 75 °C. Sensor's response has been observed to be ~10% for 1ppm of hydrogen. With increasing hydrogen concentration from 1ppm to 100 ppm, sensor response increases from ~10% to ~22.12%.
It is also observed that the increase in hydrogen concentrations leads to decrease in the sensor's response time from few hundreds of second to few second.

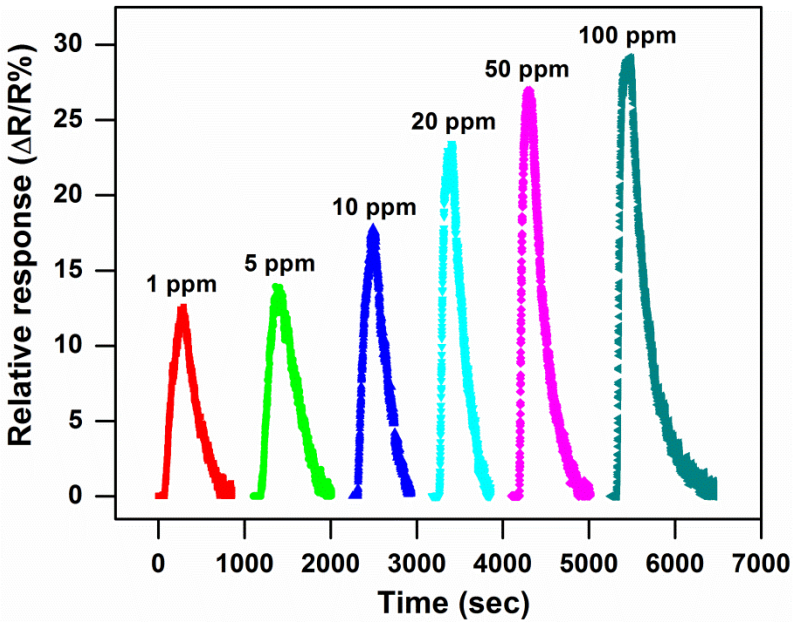

Figure 4.10: 4% Ni- doped ZnO based sensor relative response with increasing hydrogen concentration from 1ppm to 100 ppm at 75 °C

4.8 CALCULATION OF ACTIVATION ENERGY

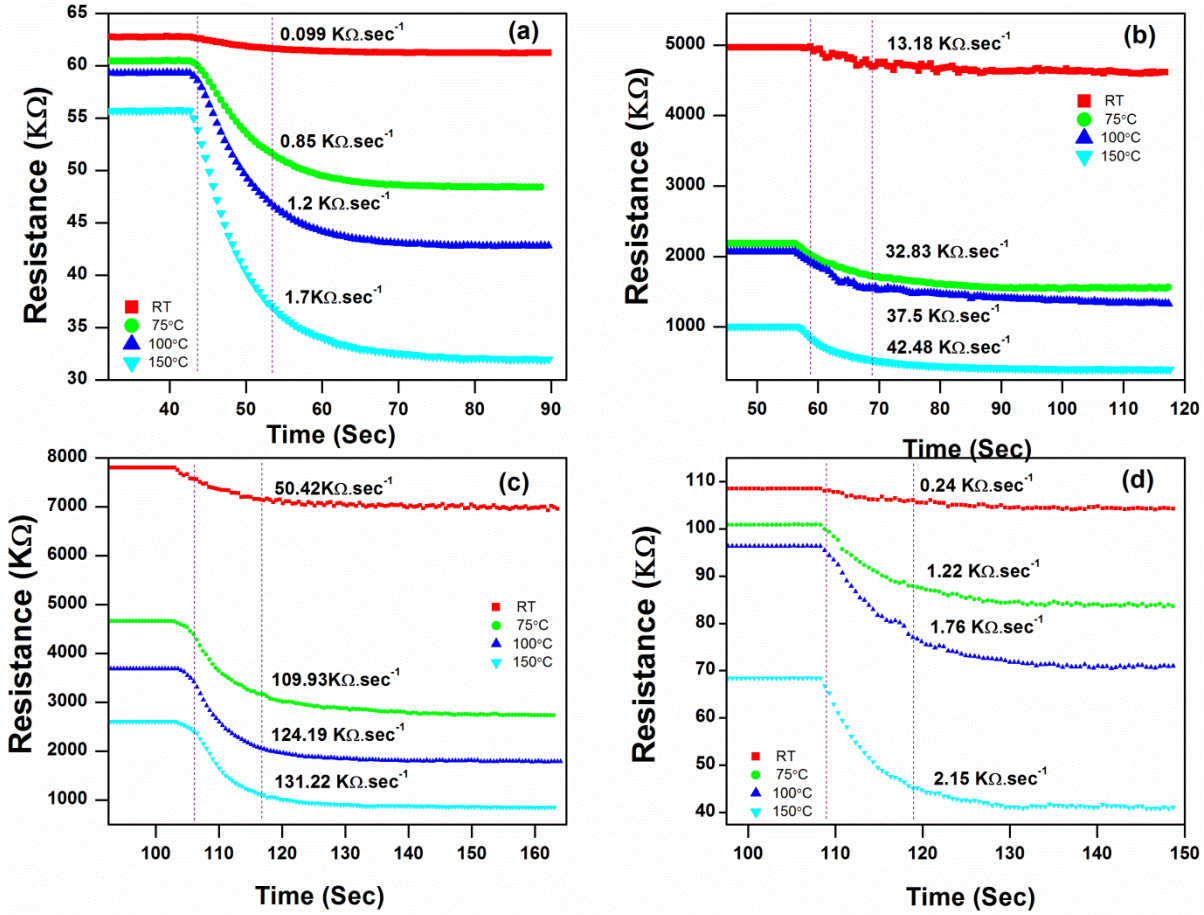

Figure 4.11: (a-d) Temperature dependent resistance v/s time curve for undoped, 2%, 4%, and 6% Ni- doped ZnO nanostructures based sensor on exposure of 1% hydrogen with operating temperature ranging from RT to 150 °C

In order to compute adsorption activation energy for 1% hydrogen gas; first of all temperature dependent resistance v/s time curves have been plotted for all the samples, which can be seen in Figure 4.11 (a-d).

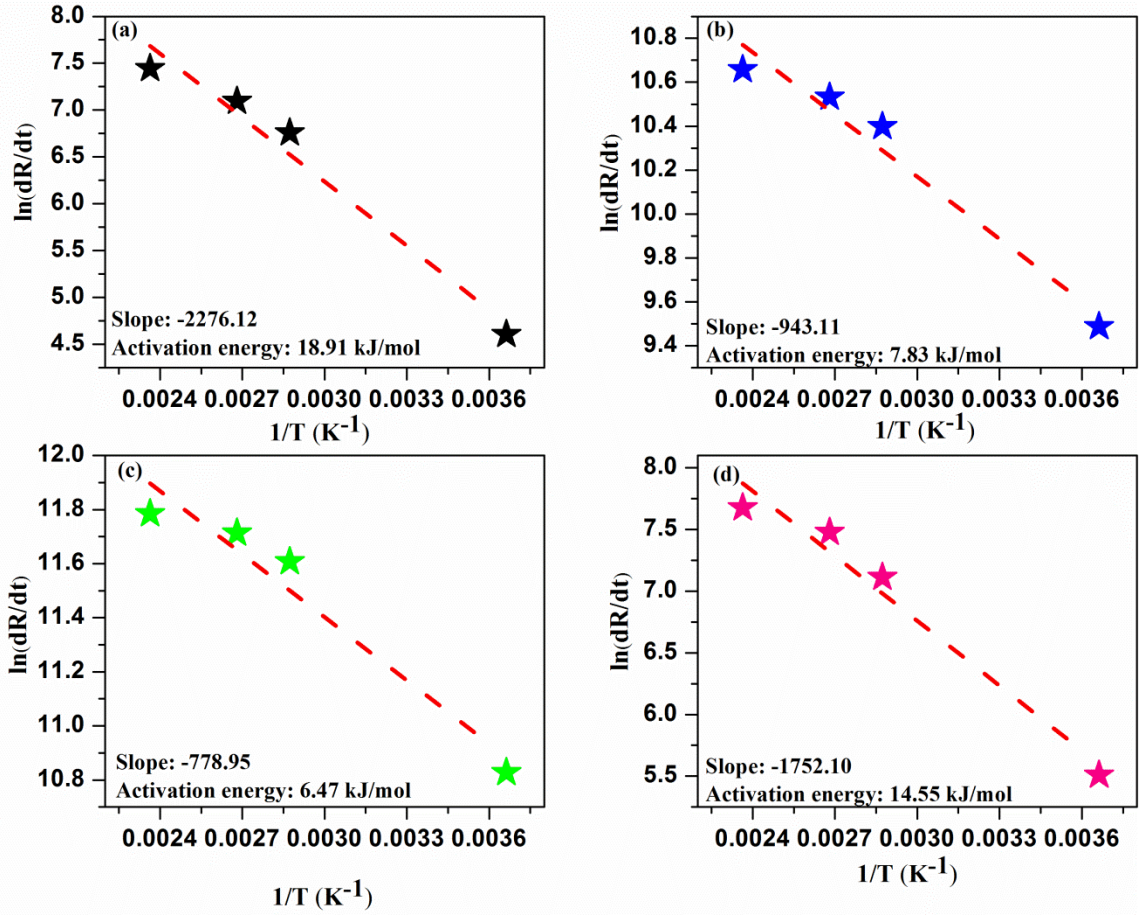

Figure 4.12: (a-d) Rate of change in resistance with temperature for undoped, 2%, 4%, and 6% Ni- doped ZnO nanostructures, respectively

Calculated activation energy has been observed to be 18.91kJ/mol, 7.83kJ/mol, 6.47 kJ/mol, and 14.56kJ/mol for undoped, 2% Ni, 4% Ni, and 6% Ni- doped ZnO nanostructures, respectively in Figure 4.13.

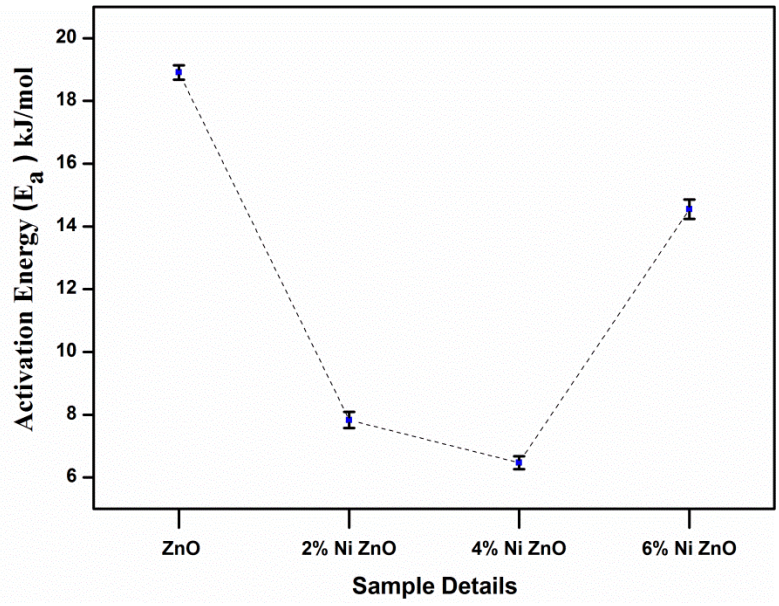

Figure 4.13: Activation energy plot for undoped and Ni- doped ZnO nanostructures

For selectivity test, the relative response of hydrogen gas has been compared with other reactive gases like CH_4, H_2S, and CO_2. Figure 4.14 shows the selectivity histogram for undoped ZnO and 4% Ni doped ZnO nanostructures based sensor for 5ppm of H_2, CH_4, H_2S, and CO_2 gases at 150 °C.

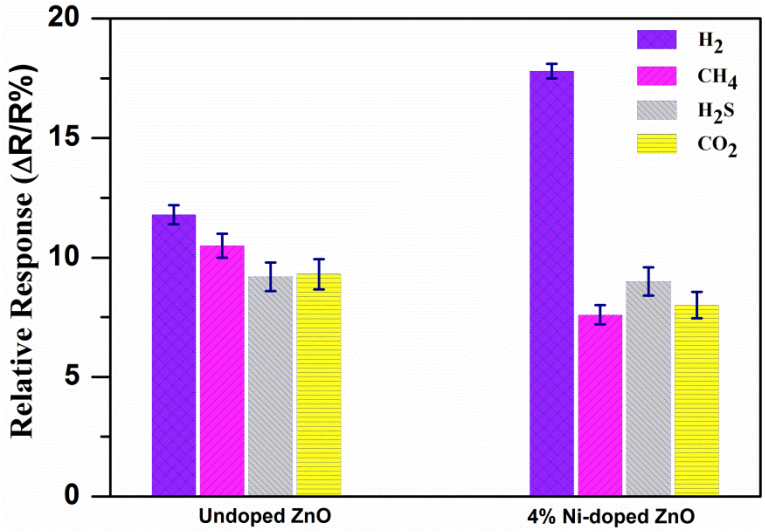

Figure 4.14: Selectivity test of different target gases for 5 ppm concentration at 150°C operating temperature

Undoped ZnO nanostructure based sensor does not show selectivity for 5ppm hydrogen gas concentration as compared to other reactive gases. In contrast to undoped ZnO nanostructure based sensor, 4% Ni doped ZnO nanostructure exhibits a remarkable H_2 response (~ 17.8 %) with a weak response (~ 7.4 for 9.11%) for other gases. This validates the selectivity of the sensor towards hydrogen gas even at lowest gas concentration (5ppm).
A comparison of sensing performance of several sensors for hydrogen with different morphology and transition metal doping has been listed in Table 4.1. While making comparison with other reported doped ZnO sensors, RF sputtered Ni doped ZnO nanostructures manifest moderate sensor response even at lower working temperature range.

Table 4.1: Comparison of hydrogen sensing performance of various metal doped ZnO sensors

Sl No.	*Sample*	*H_2 concentration (ppm)*	*Working temperature (°C)*	*Response (S)*	*Reference*
1	ZnO p-n homojunction	1000	400	1.15[a]	Hazra *et al.*, 2006
2	1D ZnO nano-assemblies	5000	400	12[a]	Barreca *et al.*, 2010
3	Mg doped ZnO film	5000	300	50[a]	Liu *et al.*, 2011
4	Co- doped ZnO nanorods	3000	150	53.7%[c]	Sett *et al.*, 2017
5	Cr- doped ZnO nanowhiskers	100	37	47[a]	Renitta *et al.*, 2016

6	ZnO nanobelt	10000	385	14.3[a]	Sadek *et al.*, 2007
7	rGO/ZnO composite	200	150	3.5[a]	Anand *et al.*, 2014
8	In –doped ZnO thin film	1	350	5%[b]	Pati *et al.*, 2015
9	Pd decorated ZnO nanosponge	20000	20	82[a]	Zhao *et al.*, 2015
10	Cd doped ZnO nanorods	500	150	2.6[d]	Yang *et al.*, 2015
11	Ni doped ZnO nanostructures	10000 5	150 150	69%[b] 17.77%[b]	This work

[a] $S = R_a/R_g$, [b] $S = (R_a-R_g)/R_a \times 100\%$, [c] $S = (I_g-I_a)/I_a \times 100\%$, [d] $S = R_{N2}/R_g$

The sensor is able to detect 5 ppm hydrogen concentration having 17.7% sensor response at 150 ^oC due to doping. Hence, these optimized Ni doped ZnO nanostructures are efficient enough to sense lowest amount of hydrogen concentration (1 ppm, 5 ppm) at mild temperature ranging from (RT to 150 ^oC) with high selectivity towards hydrogen as compared to other samples. Highest relative sensor response for 4% Ni- doped ZnO sensor is due to lowest adsorption activation energy which leads to fast adsorption/desorption reaction on the sensor's surface along with large change in the depletion region of the sensor. Hence, it is very obvious from the relative response curve that Ni content greatly increases the sensing response and reduces the operating temperature of the sensor down to 75°C than undoped ZnO. Moreover, the major role of Ni doping is to produce more active sites for chemisorbed oxygen on the sensor's surface, and correspondingly enhance its sensing response [Zhao *et al.,* 2011; Lin *et al.,* 2017].

4.9 GAS SENSING MECHANISM

In addition to gas sensing mechanism for MO_x materials, the sensing response of Ni-doped ZnO based sensors are strongly dependent upon the rate of adsorption of oxygen ions. This is also affected by operating temperature. Once chemisorbed oxygen ions are adsorbed on Ni-doped ZnO, hydrogen releases free electrons to the conduction band of ZnO nanostructures during exposure to hydrogen. Therefore, the sensor's resistance and depletion region reduces. The sensor's response is strongly correlated with the adsorption activation energy, Ni concentration, hydrogen concentration, and presence of active site. Gas sensing (adsorption/desorption of oxygen) properties of MO_x have been highly affected by surface area as well as structural defects. As the Ni doping concentration increases up to 4% in ZnO nanostructures, surface area increases due to the transformation of nano-grain structures in undoped ZnO into nano-plates with increased surface area. This might be one of the causes of enhancement in sensor's response for 4% Ni doped ZnO nanostructures. The other key factors for increased number of active sites may be related to structural defects (clearly seen in CL). Here, structural defects act as active sites and charge transfer to adsorbed oxygen ions leading to more hydrogen reactions. Thus, 4% Ni doped ZnO nanostructures reveal highest sensor response as compared to undoped ZnO nanostructures.

4% Ni-doped ZnO makes tremendous enhancement in relative response which may be due to the following factors: (i) Number of active sites for adsorption of oxygen ions increases the thickness of depletion layer by giving more amount of electrons from conduction band of Ni-doped ZnO nanostructures (ii) lower activation energy enhances adsorption/desorption reaction kinetics to 4% Ni-doped ZnO nanoplates which results in the enhancement of current due to reduction in barrier height during exposure to H_2 gas. On the other hand, 6% Ni doping displays a decrease in relative response because of the change in growth direction of ZnO as well as its degraded crystallinity. Apart from this, the activation energy has been found to be higher than 4% Ni-doped ZnO, causing less adsorption/desorption reaction on the sensor's surface and decrease in the relative response.

4.10 CONCLUSION

In the conclusion of this chapter, undoped and Ni doped (2, 4, and 6% Ni) ZnO nanostructures have been deposited by RF magnetron sputtering system. XRD pattern reveals hexagonal wurtzite structure for undoped and Ni-doped ZnO. In undoped ZnO, preferential growth is observed along with the c-axis. Secondary phase of NiO has been detected for 6% Ni-doped ZnO. FESEM shows the columnar structure having conical tips of very dense packed ZnO nanorods for undoped ZnO nanostructures. However, the surface morphology transforms with the Ni doping. High resistance of 4% Ni- doped ZnO is due to higher barrier height between metal and ZnO as well as between columnar structures having the shape of nanoplates. The highest relative response is observed for 4% Ni-doped ZnO nanostructures. Lower limit of detection is also possible down to 1ppm (~10%) at moderate operating temperature (75 ^{o}C) and the stability sustains up to 150 days without reduction in relative response for 4% Ni-doped ZnO sensor. Excellent relative response is observed for 4% Ni-doped ZnO sensor, caused by large surface sites for adsorption of oxygen on nanoplates, and lowest activation energy ~6.47 KJ/mol. Lastly, the reduction in relative response for 6% Ni- doped ZnO is due to the modification in growth direction of ZnO crystal structures.